Improving D-2-hydroxyglutarate MR spectroscopic imaging in mutant isocitrate dehydrogenase glioma patients with multiplexed RF-receive/B0-shim array coils at 3 T

Bernhard Strasser[1,2], **Nicolas S. Arango**[3], **Jason P. Stockmann**[1,4], **Borjan Gagoski**[5,6], **Bijaya Thapa**[1], **Xianqi Li**[1], **Wolfgang Bogner**[2], **Philipp Moser**[2], **Julia Small**[7], **Daniel P. Cahill**[7], **Tracy T. Batchelor**[8], **Jorg Dietrich**[8], **Andre van der Kouwe**[1,4], **Jacob White**[3], **Elfar Adalsteinsson**[3,9], **Ovidiu C. Andronesi**[1,4]

[1]A. A. Martinos Center for Biomedical Imaging, Massachusetts General Hospital, Radiology, Boston, Massachusetts, USA

[2]High-Field MR Centre, Department of Biomedical Imaging and Image-Guided Therapy, Medical University of Vienna, Vienna, Vienna, Austria

[3]Department of Electrical Engineering and Computer Science, Massachusetts Institute of Technology, Cambridge, Massachusetts, USA

[4]Harvard Medical School, Boston, Massachusetts, USA

[5]Fetal Neonatal Neuroimaging and Developmental Science Center, Boston Children's Hospital, Boston, Massachusetts, USA

[6]Department of Radiology, Harvard Medical School, Boston, Massachusetts, USA

[7]Department of Neurosurgery, Massachusetts General Hospital, Boston, Massachusetts, USA

[8]Department Neurology, Division of Neuro-Oncology, Massachusetts General Hospital, Boston, Massachusetts, USA

[9]Institute for Medical Engineering and Science, Massachusetts Institute of Technology, Cambridge, Massachusetts, USA

Abstract

MR spectroscopic imaging (MRSI) noninvasively maps the metabolism of human brains. In particular, the imaging of D-2-hydroxyglutarate (2HG) produced by glioma isocitrate dehydrogenase (IDH) mutations has become a key application in neuro-oncology. However, the performance of full field-of-view MRSI is limited by B_0 spatial nonuniformity and lipid artifacts

from tissues surrounding the brain. Array coils that multiplex RF-receive and B_0-shim electrical currents (AC/DC mixing) over the same conductive loops provide many degrees of freedom to improve B_0 uniformity and reduce lipid artifacts. AC/DC coils are highly efficient due to compact design, requiring low shim currents (<2 A) that can be switched fast (0.5 ms) with high interscan reproducibility (10% coefficient of variation for repeat measurements). We measured four tumor patients and five volunteers at 3 T and show that using AC/DC coils in addition to the vendor-provided second-order spherical harmonics shim provides 19% narrower spectral linewidth, 6% higher SNR, and 23% less lipid content for unrestricted field-of-view MRSI, compared with the vendor-provided shim alone. We demonstrate that improvement in MRSI data quality led to 2HG maps with higher contrast-to-noise ratio for tumors that coincide better with the FLAIR-enhancing lesions in mutant IDH glioma patients. Smaller Cramér–Rao lower bounds for 2HG quantification are obtained in tumors by AC/DC shim, corroborating with simulations that predicted improved accuracy and precision for narrower linewidths. AC/DC coils can be used synergistically with optimized acquisition schemes to improve metabolic imaging for precision oncology of glioma patients. Furthermore, this methodology has broad applicability to other neurological disorders and neuroscience.

Keywords

D-2-hydroxyglutarate; glioma brain tumor; isocitrate dehydrogenase mutations; magnetic resonance spectroscopic imaging; multicoil shimming; multiplexed RF-receive and B0-shim array; precision oncology

1 | INTRODUCTION

Spatial mapping of brain metabolism by 3D MRSI provides comprehensive evaluation of tumor burden with higher specificity than anatomical imaging, which is valuable to guide treatment planning and assess treatment response.[1–5]

D-2-hydroxyglutarate (2HG) is an oncometabolite produced by tumors with point mutations in the isocitrate dehydrogenase (IDH) enzymes IDH1 and IDH2.[6] IDH mutations are highly frequent in lower grade gliomas[7] and produce high concentrations (>1 mM) of 2HG, which can be used as a biomarker for diagnosis and monitoring of tumor evolution. In vivo MRS can noninvasively measure 2HG concentrations in mutant IDH glioma patients,[8–11] which has become a key clinical application in neuro-oncology.

Although 2HG theoretically has a very high contrast-to-noise ratio (CNR) between mutant IDH tumor and healthy brain where it is virtually absent, the detection of 2HG by in vivo MRS is complicated by low signal-to-noise ratio (SNR), and spectral overlap with abundant brain metabolites such as glutamate, glutamine, myo-inositol, and creatine. Optimized sequences for 2HG measurements at 3 T have been introduced,[3,8–16] but the ability to fit and separate 2HG from the brain metabolic background critically depends on spectral quality. Spectral linewidths of narrower than 0.1 ppm are required, which is the separation between 2HG and glutamate and glutamine. This requirement is challenging to fulfill uniformly over the entire brain due to local B_0 inhomogeneities, and it is even more challenging in brain tumor patients due to blood in the tumor, surgical cavities, or metal implants postsurgically.

Additionally, the SNR of the 2HG signal is low, and to boost SNR large voxels or long measurement times are necessary. While long measurement times (>10 min) are prohibitive in routine clinical investigations, low spatial resolution leads to strong lipid artifacts for unrestricted field of view (FOV) MRSI, especially if no outer-volume suppression methods are employed, thereby preventing reliable 2HG quantification. On the other hand, restricting the FOV by inner volume selection and outer-volume suppression provides only partial brain coverage, is difficult to prescribe, and misses tumor regions towards the brain periphery.

Methods that correct B_0 inhomogeneity using active shimming[17–23] or during postprocessing[24–26] can improve MRSI data quality. In cases of severe B_0 distortions, the use of advanced shimming hardware with high order spherical harmonics[18] or multicoil arrays[19] is indispensable to adequately recover spectral linewidth. Integrated radio frequency (RF)-receive and B_0-shim coil arrays[20,21] multiplex AC and DC electrical currents through the same set of conductive wire loops to simultaneously receive RF signal (AC) and generate independent B_0 spatial field patterns (DC). They provide degrees of freedom for high spatial order B_0 shimming in the brain,[19,27] supplementing the scanner's standard second-order spherical harmonics (2SH) shim, while maintaining the high RF-receive sensitivity of the 32-channel receive array. Hence, such AC/DC coil arrays enable improved linewidths over large brain volumes for 3D MRSI, as has been recently shown at 7 T.[28,29] As a result of their small size, low inductance, and distance to conductive metal structures in the bore, these shim coils can be switched rapidly within a single TR[28] without inducing eddy currents. This allows B_0 field patterns to switch and alternate between lipid suppression and metabolite acquisition to maximize the performance of each sequence module. Shaping the B_0 field in the scalp during lipid suppression, either to shift the fat frequency[28,30] or to spoil the fat signal,[31] has been shown to reduce lipid artifacts in MRSI. Thus, by simultaneously improving linewidths and lipid suppression, AC/DC coils enable 3D MRSI over a thick brain slab at a spatial resolution that optimizes scan time, SNR, and linewidths for a clinically feasible protocol.

Based on simulations, we hypothesized that the ability to detect and quantify 2HG from 3D MRSI in mutant IDH glioma patients will be improved by using an AC/DC coil. Motivated by the high clinical value of 2HG imaging for glioma patients, we demonstrate the feasibility of first clinical applications of AC/DC coils.

2 | EXPERIMENTAL

Our methodology was developed and implemented on a 3-T Skyra scanner (Siemens Healthcare, Erlangen, Germany). Details of the pulse sequence are presented in Figure 1.

2.1 | Multicoil shimming hardware and software

We employed recently developed multicoil dynamic shimming hardware consisting of a 32-channel "AC/DC" coil array patterned on a 3D printed helmet, as described in[20] (Figure 1A). The helmet is 22.5 cm high in the A/P, and 19 cm wide in the R/L dimension, which fits about 90% of the healthy adult population. RF-receive loops with a diameter of 9.5 cm made of AWG16 solid wire are arrayed in a hexagonal–pentagonal pattern, with critical overlap to decouple neighboring elements. Toroidal inductive chokes are used to bridge

DC shim current into each RF-receive loop, thus adding B_0 field control capability to each element in the array. In this way, the array provides both RF-receive and B_0 shimming functionality with high efficiency by placing the loops close to the brain, where they operate with high efficiency for both signal reception and generating B_0 field offsets. Shim currents were driven by a bank of digitally programmable low-voltage amplifiers that allows very fast switching under 1 ms between different B_0 field offsets.[28,32] The output stage devices are mounted to heat sinks with in-laid piping for optional water cooling. For further details of the AC/DC array hardware and shim amplifiers, we refer the reader to the references,[20,32] respectively.

For MRSI measurements, the AC/DC shims were dynamically switched between a metabolite homogeneity B_0 shim ($ACDC_{met}$) during data acquisition, and a fat suppression B_0 shim ($ACDC_{fat}$) during fat suppression. Whenever these two fields are dynamically switched within the same sequence, they are referred to as $ACDC_{met|fat}$. The $ACDC_{met}$ and $ACDC_{fat}$ were independently optimized on top of the 2SH shim. Because the different shims are calculated for different volumes, we further indicate the shim volume by appending "Box", "Brain", or "Scalp" to the shim names as subscripts (e.g. $2SH_{Box}$ + $ACDC_{metBrain|fatScalp}$). The "Box" shim is a rectangular volume that covers the whole excited slab, and includes the brain, scalp, and skull. The "Brain" shim volume includes only the brain without the skull or scalp, while the "Scalp" shim volume includes only the fat-containing scalp layer.

For calculating the $2SH_{Box}$ shim, three shim-iterations with the manufacturer's dual echo steady state (DESS) sequence were used. Empirically, using several shim-iterations improves the B_0-homogeneity in comparison with a single iteration. For calibrating the AC/DC shim coils, a standard two-echo gradient echo B_0 mapping sequence was used to measure the B_0-fields caused by each individual AC/DC shim coil in a large phantom. During the subject measurements, B_0 fieldmaps were measured after applying the $2SH_{Box}$ shim using the same sequence. The phase difference image was spatially unwrapped with FSL PRELUDE[33] and converted to a B_0-fieldmap. The optimal shim currents for the 32 shim channels were computed using offline custom optimization software implemented in MATLAB (MathWorks, Natick, MA, USA). A single shim-iteration was performed as follows. For the $ACDC_{metBrain}$, DC shim currents were calculated using a least squares penalty on the remaining B_0 (after shimming with the 2SH-shim) with the goal of minimizing the standard deviation of the B_0 within the shim volume. The linearly constrained, quadratic objective optimization problem for brain homogeneity is solved using MATLAB's built-in quadratic program solver, quadprog. The convex, linear optimization problem for lipid suppression is solved using MATLAB's linear program solver, linprog (more details are given in Supplementary Information). Shim currents were automatically calculated in less than 1 min through solution of the optimization problems.

When using the 2SH-shim as a preshim for the $ACDC_{metBrain}$, a higher B_0-homogeneity can be achieved than when using only the $ACDC_{metBrain}$, with the disadvantage of increasing the preparation time. The three shim iterations for the 2SH preshim took about 80–120 s in total, while both ACDC shims (measurement + calculation time) took about 130 s, resulting in a total time of about 210 s. However, the calculation of the 2SH-shims and ACDC-shims

could be performed simultaneously, and based on the same B_0-maps, which would almost eliminate the additional time demand of the 2SH preshim. For the $ACDC_{fatScalp}$, the DC currents were jointly optimized along with the transition frequency of the lipid suppression pulse, with the goal of minimizing the number of voxels containing unsuppressed lipids in the scalp compartment and incidentally suppressed NAA in the brain compartment. This procedure has the effect of widening the spectral interval between spatially separated lipids and NAA beyond their intrinsic 0.7-ppm gap. More details can be found in supporting information file S1. Figure 1C illustrates such an increased spectral gap between the 1.3-ppm lipid peak and NAA, while supporting information file S2 shows the case for the 2.24-ppm lipid peak. The application of the $ACDC_{fatScalp}$ and $ACDC_{metBrain}$ shims was triggered dynamically within each TR by the pulse sequence, as shown in Figure 1B.

In summary, our proposed shim methodology consists of four components: (1) the standard 2SH-shim, which provides the constant "baseline" shim; (2) the AC/DC coil, which adds localized B_0 fields; (3) the capability to dynamically switch those AC/DC fields within each TR, allowing to separately optimize the shim for metabolite detection and lipid suppression; and (4) our shim software, which more readily than the scanner's shim software allows to shim only the brain instead of the whole head.

2.2 | Data acquisition and processing

Our MRSI sequence[34] used an adiabatic spin-echo (ASE) excitation for axial slab selection and a stack-of-spirals for 3D k-space encoding, as shown in Figure 1B. Because ASE is double refocusing, similar to PRESS, we optimized it for 2HG detection using TE1/TE2 = 32/65 ms.[9] We verified by simulations (Figure 2) that ASE at TE = 97 ms produces 2HG phase modulations similar to PRESS at TE = 97 ms, as described by Choi et al.[9] ASE uses adiabatic RF pulses of larger bandwidth compared with PRESS, and which reduce the chemical shift displacement error by 20-fold, provide more uniform and sharper slab excitation, and also compensate for B_1 inhomogeneity. The ASE used a BIR-4 adiabatic excitation pulse[35] and two adiabatic gradient offset independent wideband uniform rate and smooth truncation (GOIA-W)(16,4) refocusing pulses.[36] Lipid suppression was achieved with inversion recovery using a hypergeometric single band (HGSB) pulse[37] for selective adiabatic inversion of the main lipid peaks at 1.3 and 0.9 ppm. An inversion time (TI) of 210 ms was used for fat nulling, which is close to the TI used at 3 T.[38] The HGSB pulse had a wide inversion bandwidth of 2 kHz and a narrow transition band of 48 Hz (0.4 ppm at 3 T), which is smaller than the separation (0.7 ppm) between the main peaks of NAA (2 ppm) and lipids (1.3 ppm). The wide inversion bandwidth is necessary, because the $2SH_{Box}$ + $ACDC_{fatScalp}$ broadens the lipid frequency range. Details regarding all the pulses can be found in the supporting information file S3.

The HGSB inversion profile and histogram of NAA and fat frequencies are shown in Figure 1C. As a result of the widened NAA-fat gap, the HGSB transition band hardly overlaps with the fat frequencies in the case of the $2SH_{Box}$ + $ACDC_{fatScalp}$, while it partially overlaps for the $2SH_{Box}$ shim. The center of the HGSB transition band was set to 1.6 ppm for 2SH shimming, providing no inversion above 1.8 ppm and full inversion below 1.4 ppm. For the $2SH_{Box}$ + $ACDC_{fatScalp}$ shim, the center frequency of the HGSB pulse was set

according to the measured frequency shift of the fat layer with the optimized $2SH_{Box}$ + $ACDC_{fatScalp}$ applied. After HGSB lipid inversion and before water suppression, the AC/DC coil was switched to the $ACDC_{metBrain}$ shim, which was maintained during metabolite excitation and acquisition until the next HGSB pulse. The water suppression enhanced through T_1 effects (WET)[39] was inserted during the inversion recovery TI, and immediately before the beginning of the ASE excitation. The following sequence parameters were used: TE1/TE2/TR/TI = 32/65/1800/210 ms, 3D stack-of-spirals (maximum gradient amplitude per direction: 11.09 mT/m, maximum slew rate per direction: 127 mT/m/ms), FOV 240 $\times$ 240 $\times$ 100 mm^3, volume of interest 240 $\times$ 240 $\times$ 50 mm^3, matrix size 24 $\times$ 24 $\times$ 10, nominal voxel size 1 cm^3, 1100 Hz spectral bandwidth, two temporal interleaves, four angular interleaves, four averages (cosine-weighted in z-direction), and a total acquisition time of 5 min 24 s. In all subjects, the shim volumes were similarly chosen.

In addition to previous work,[28] we inserted an interleaved EPI-based volumetric navigator into our 3D MRSI sequence, which was played every TR before lipid inversion for real-time motion and frequency drift correction.[40]

B_0-fieldmaps and anatomical imaging with FLuid-Attenuated Inversion Recovery (FLAIR), and multiecho-MPRAGE (MEMPRAGE),[41] were also acquired. B_0-fieldmaps were acquired with a 2D two-echo gradient echo sequence with a resolution of 2 $\times$ 2 $\times$ 2 mm^3, slice gap of 2 mm, FOV of 220 $\times$ 220 $\times$ 160 mm^3, and TEs of 5 and 7.46 ms. The ΔTE of 2.46 ms ensures that water and the main lipid peak around 1.3 ppm are in phase at 3 T, so that the chemical shift between water and the primary lipid peak does not influence the image phase and thus the derived ΔB_0-maps.

All MRSI data were phase-corrected to account for the fact that different spiral k-space points were acquired at different time points[42] and density-compensated in k-space.[43] Afterwards, the data were gridded to Cartesian k-space points using a Kaiser–Bessel kernel,[44] Fourier-transformed, coil combined using a sensitivity map, Hamming-filtered in the in-plane k-space, and finally processed with LCModel.[45] The Hamming filter increased the effective voxel size by a factor of 1.53 over the effective unfiltered size. Default LCModel parameters were used to fit the 1.8–4.2 ppm range, except that LCModel was not allowed to simulate peaks, the uncertainty of the zero- and first-order phases were set to 20, and the residual water peak was used for estimating the frequency shifts. A basis set for ASE was simulated in GAMMA[46] (supporting information file S4). Metabolic maps were converted to pseudo-absolute concentrations by taking the mean total creatine (tCr) signal scaled by the slice-by-slice gray and white matter distribution, while assuming a tCr concentration of 7 mmol/kg in white and 8.6 mmol/kg in gray matter.[47] The tCr concentration was also compared between the tumor and the normal appearing brain to test whether tumors could pose a problem for these assumptions. Brain segmentation was performed on the anatomical images using FAST,[48] and the segmented images were downsampled in k-space and Hamming-filtered to match the MRSI acquisition. All voxels of all slices within the volume of interest and with CSF contributions of less than 50% were analyzed in quantitative comparisons.

2.3 | Spectral simulations

All simulations for the ASE spectra were performed using the GAMMA[46] library, and using the same exact waveform modulations for all RF and gradient pulses, and the echo times as played by the scanner during the ASE pulse sequence. During the RF pulses the spin evolution was calculated with the time-dependent Liouville–von Neumann density matrix equation using a piece-wise constant Hamiltonian with a time step of 10 μs, which is the same as the gradient raster-time of the scanner. We verified that the 10-μs time step was sufficient in simulations and produced the same results with shorter time steps of 1 μs. The NMR interactions (chemical shift and scalar couplings) corresponding to the spin system of each metabolite were used from the literature.[49,50]

To account for localization and slice profile errors of the GOIA pulses, a slab of 50-mm thickness was assumed to be selected in the middle of a one-dimensional, 100-mm long object. The object was divided into 1000 very thin sections. The number of thin sections was verified to be sufficient as further increases did not change the results. Note that a one-dimensional object is appropriate because the pair of GOIA pulses is used to select only along the slice direction. The offset (γzG) induced by the gradient was considered to be constant across an infinitesimal section and the spin evolution was calculated independently for each section, and finally the spectra from all the sections were averaged. Spectra were simulated assuming the same spectral window (dwell time) as used during acquisition, and the same carrier frequency for all the RF pulses. To speed up the simulations we used the symmetry of the RF and gradient waveforms.

2.4 | Study design and data evaluation

In a first series of tests we investigated through simulations how reliably 2HG can be fitted in tumor spectra depending on the spectral linewidth. In the second series of tests, we compared our proposed shim methodology with the vendor-provided shim. In total, nine human subjects were imaged for testing, as detailed below.

For the first series of tests, we performed simulations of brain tumor spectra for different spectral linewidths, assuming ASE excitation. Synthetic tumor spectra were obtained by combining simulated spectra of 14 brain metabolites and 2HG (supporting information file S5). Two cases were considered for 2HG concentration: 2 and 5 mM. To mimic the effects of B_0 inhomogeneity, we applied line broadening in the range of 0.008–0.243 ppm with a 0.008-ppm step size; 10% white noise was added after line broadening in all simulations. The simulated spectra were fitted with LCModel[45] equivalently to experimental spectra. The 2HG Cramér–Rao lower bounds (CRLB) and the 2HG concentration error between the fitted and the ground truth values were investigated.

For the second set of comparisons performed in all subjects, the MRSI sequence and B_0-maps were measured twice under two different shimming situations: (1) using $2SH_{Box}$ shimming, and (2) using the dynamic $2SH_{Box} + ACDC_{metBrain|fatScalp}$. This comparison was deemed the most relevant because it compares the AC/DC shimming with the manufacturer shimming available to all users. Due to time restrictions, volunteer 4 and patient 4 were only measured with $2SH_{Box}$ and $2SH_{Box} + ACDC_{metBrain}$ shims. To

characterize improvements in spectral quality, several metrics were used: (1) linewidths; (2) SNRs; (3) CRLB of 2HG estimated by LCModel; and (4) lipid content, estimated by summing the magnitude spectra in the range 2.3–0.3 ppm. Wilcoxon rank-sum tests were used to test for statistical differences between both shim conditions. To characterize improvements in 2HG image quality, the following metrics were used: (1) the coefficients of variation (CVs) of 2HG inside and outside of tumors; and (2) the contrast-to-noise ratio,

$$CNR = \frac{mean(2HG_{Tumor}) - mean(2HG_{Background})}{std(2HG_{Background})}$$, where background represents the normal

appearing brain outside the tumor. Tumor regions were outlined on the FLAIR images.

Furthermore, we investigated the contribution of the shim volume for improving B_0 shimming and the shimming repeatability (supporting information files S6 and S7).

2.5 | Human subjects

Five healthy control volunteers and four mutant IDH1 glioma patients (two males and two females, aged 28, 31, 34, and 41 years) were measured to test our methodology. All four patients had IDH-mutated tumors, as confirmed by immunohistochemistry.[51] Informed consent was obtained from each subject, and the local institutional review board approved the study. Patient 1 had an IDH1-R132H mutated glioblastoma, which was partially resected 2 weeks before the measurement. This patient posed challenges for MRSI by postsurgical changes that strongly decreased B_0-homogeneity in the residual tumor due to a large accumulation of blood products in the surgical cavity, and a large titanium metal plate for skull repair. Patient 2 was scanned one day presurgically and presented with a small FLAIR lesion that was confirmed postsurgically to be a diffuse astrocytoma with IDH1-R132H mutation. However, this patient had very low mutant IDH1 cell density by immunohistochemistry staining, suggesting an early-stage tumor with very low 2HG concentrations.[4] In both patients 1 and 2, the tumor had a frontal location at the anterior pole close to the frontal sinuses, which is very challenging for B_0 shimming. Patient 3 had a fronto-parietal residual tumor postsurgery, and patient 4 had a temporal tumor presurgically.

3 | RESULTS

The effects of increasing linewidths on the 2HG fitting are shown in Figure 2 for simulated spectra. For narrow linewidths of 0.081 ppm or less, a rich spectral pattern can be observed in the 2.1–2.5 ppm range (Figure 2A,B). For broad linewidths of 0.138 ppm or more, the characteristic spectral pattern is lost by blurring and partial signal cancellation. The specific 2HG signal at 2.25 ppm is not fitted at all in broad spectra for 2 mM concentration (Figure 2A, bottom row). The effects of linewidth on 2HG quantification errors are shown in Figure 2C,D. The relative CRLB (Figure 2C) remain under 20% for linewidths of less than 0.1 ppm, but sharply increase at linewidths of 0.12 ppm or more for 2 mM concentration, and for linewidths of 0.15 ppm or more for 5 mM concentration. The ratio between estimated and true concentrations (Figure 2D) is closer to 1 for linewidths of less than 0.12 ppm and approaches 0 for increasing linewidths. The detrimental effect of increasing linewidths is more pronounced at low 2HG concentrations, and the ability to estimate 2 mM is completely compromised for linewidths of 0.12 ppm or more.

Figure 3 shows the B_0-maps of patient 2, together with the linewidth map, and examples of spectra for the standard $2SH_{Box}$ and the $2SH_{Box} + ACDC_{metBrain|fatScalp}$ shim conditions. Improvements in spectral quality with the $2SH_{Box} + ACDC_{metBrain|fatScalp}$ are visually obvious. The example of the $2SH_{Box}$ spectrum #1 displays a broad linewidth that results in a large peak overlap of tCr at 3.0 ppm and total choline at 3.2 ppm. By contrast, the $2SH_{Box} + ACDC_{metBox|fatScalp}$ spectrum #1 shows a narrower linewidth with clearly separated peaks. In addition, both spectra show examples where the improved lipid suppression by the $2SH_{Box} + ACDC_{metBrain|fatScalp}$ shimming results in a flatter baseline in comparison with the $2SH_{Box}$ shim.

Quantitative analysis revealed that the average linewidth decreased by 19% from 0.103 ± 0.046 to 0.083 ± 0.044 ppm ($p < 0.001$) for patients, and by 18% from 0.091 ± 0.041 to 0.074 ± 0.036 ppm ($p < 0.001$) for volunteers. The average SNR slightly increased from 13.5 ± 6.4 to 14.2 ± 6.4 ($p < 0.05$) for patients, and by 9% from 16.1 ± 6.9 to 17.6 ± 6.7 ($p < 0.001$) for volunteers. The lipid content inside the brain decreased by 23% on average for patients ($p < 0.001$), and by 21% for volunteers ($p < 0.001$), when using the $2SH_{Box} + ACDC_{metBrain|fatScalp}$ versus the $2SH_{Box}$ shimming. It is important to realize that these are not the absolute lipid suppression factors (i.e. not the comparison of fat suppression with no suppression), but the improvements with the $2SH_{Box} + ACDC_{metBrain|fatScalp}$ over the $2SH_{Box}$ shim. Examples of lipid maps are shown in Figure 4.

The tCr concentrations in the tumor were estimated to be 6.7 ± 2.1 mM, while outside of the tumor they were 6.3 ± 1.9 mM. Both values seem to be slightly affected by CSF, but are very similar.

Figure 5 shows the 2HG concentration and CRLB maps of patients 1, 3, and 4 together with the FLAIR images in transversal and sagittal views. The shim volumes are indicated by green (box and metBrain) and red (fatScalp) overlays over the FLAIR images. The resection cavity of patient 1 has very bright FLAIR contrast due to blood products from the surgery. In the case of $2SH_{Box} + ACDC_{metBrain|fatScalp}$ of patient 1, an area of high 2HG with low CRLB values can be clearly seen in the residual tumor tissue located posterior and superior to the surgical cavity with little background signal outside the tumor. For the $2SH_{Box}$ shim case, the area of detectable 2HG near the tumor is smaller, and there are areas with high 2HG in the anterior brain or on the contra-lateral side disagreeing with the FLAIR-enhancing tumor. Patients 3 and 4 also show 2HG increases in the tumor regions, although in patient 3 this is less pronounced than in patients 1 and 4. In the case of the 2SHBox shim condition, high 2HG coincide less with the FLAIR-enhancing regions, with high foci far away from the tumor. The error in 2HG fitting decreased in all three patients with AC/DC shimming, as the CRLB maps show lower values in the tumor area for $2SH_{Box} + ACDC_{metBrain|fatScalp}$ than for $2SH_{Box}$. The CNR of 2HG maps improved substantially from 0.11 ± 0.05 with $2SH_{Box}$ shimming to 1.45 ± 0.74 with the $2SH_{Box} + ACDC_{metBrain|fatScalp}$. The red arrows in patient 1 indicate the positions of the spectra (shown in supporting information file S8) from a voxel within the tumor and a voxel located in the healthy appearing brain from the contralateral hemisphere. These spectra demonstrate a significant improvement in quality when using the $2SH_{Box} + ACDC_{metBrain|fatScalp}$ over the $2SH_{Box}$ shim condition. The mean linewidth in the tumor

voxels of patients 1, 3, and 4 was reduced from 0.097 ± 0.037 to 0.076 ± 0.024 ppm ($p <$ 0.001). The $2SH_{Box} + ACDC_{metBrain|fatScalp}$ linewidths are in the range where simulations indicated acceptable estimation for 2HG concentration, which is confirmed experimentally here, showing a clearer 2HG signal contribution (overlaid in red). Results of the quantitative analysis are summarized in Table 1. Figure 6 shows axial 2HG maps for patient 2 and two volunteers. No 2HG increase could be detected in the tumor of patient 2 for both shim conditions, with 2HG CNR values of −0.76 for the $2SH_{Box}$ shim and −0.45 for the $2SH_{Box} + ACDC_{metBrain|fatScalp}$. In healthy subjects and patient 2, fewer areas with high 2HG concentrations were present in the healthy brain for the $2SH_{Box} + ACDC_{metBrain|fatScalp}$, resulting in fewer 2HG foci disagreeing with FLAIR-enhancing tumors. This is reflected by a decrease in the CV of 2HG by 63%. Within the tumors of patients 1, 3, and 4, the CV decreased by 40% for the $2SH_{Box} + ACDC_{metBrain|fatScalp}$. The mean 2HG CRLB inside the tumors of patients 1, 3, and 4 were below 40% only for the $2SH_{Box} + ACDC_{metBrain|fatScalp}$. For patient 2, neither shim condition achieved CRLB below 40% inside the tumor.

Figure 7 shows that the $2SH_{Box} + ACDC_{metBrain|fatScalp}$ also improves the quantification of other metabolites, such as glutamate and glutamine (Glx), NAAG, and total NAA (tNAA). With the $2SH_{Box}$ shim, random foci in the metabolic maps are visible for patient 2. With the $2SH_{Box} + ACDC_{metBrain|fatScalp}$, the metabolic maps show a better agreement with the underlying anatomical images. Volunteer 2 provides an example of where the $2SH_{Box} + ACDC_{metBrain|fatScalp}$ only modestly improved the quantification of these three metabolites, because the data quality was already sufficient in the $2SH_{Box}$ case.

Additional results related to region of interest (ROI) selection, stability, and repeatability for 2SH and AC/DC shimming, are provided in the supporting information.

4 | DISCUSSION

In this first clinical application of AC/DC coils at 3 T we showed that 3D imaging of 2HG is feasible at resolutions of 10-mm isotropic over an unrestricted in-plane FOV of the brain with the benefit of short acquisition times and high SNR, but without the usual penalties of lipid contamination or large linewidths normally associated with such resolutions. This was achieved by using an AC/DC coil in combination with an adiabatic dual-refocusing stack-of-spirals 3D MRSI sequence optimized for 2HG detection, including an interleaved volumetric navigator for real-time motion and frequency correction. We investigated the influence of the AC/DC methodology on metrics such as the global B_0-homogeneity, local spectral linewidth, SNR, and lipid suppression. The net effects of higher spectral quality were lower CRLB for 2HG quantification and a better overlap of high 2HG with the tumor regions outlined by FLAIR images in three of the four patients. Simulations indicate that 2HG is underestimated for linewidths of 0.12 ppm or more, particularly for low 2HG concentrations. This might be clinically very relevant, because low 2HG concentrations can occur in patients with incipient tumors, where early cancer detection is critical, or in patients after surgical resection, for which monitoring of residual tumor is required. The first patient that was scanned shortly after surgery posed the greatest challenges for MRSI data quality through a combination of several factors: (1) anterior pole frontal tumor location close to sinuses and air cavities; (2) large accumulation of blood products with paramagnetic

Fe2+ from deoxyhemoglobin; and (3) a titanium plate for skull repair and fiducials for radiotherapy. Due to these challenges, the $2SH_{Box}$ shim resulted in a 2HG image with high foci that disagree and are remotely outside the FLAIR-enhancing tumor. The $2SH_{Box}$ + $ACDC_{metBrain|fatScalp}$ shimming improved the 2HG maps in patients 1, 3, and 4, with higher 2HG signal in the tumor and less variability outside the tumor. With the $2SH_{Box}$ + $ACDC_{metBrain|fatScalp}$, the CNR of the tumors increased by 45% above the background, resulting in 2HG foci coinciding with the FLAIR-enhancing tumor. The second patient presented with the challenges of B_0-inhomogeneity in the frontal pole tumor location and of presumably very low 2HG levels typically seen for small tumors with a low density of mutant IDH cells,[4] as was confirmed using antimutant IDH immunohistochemistry staining. While the $2SH_{Box}$ + $ACDC_{metBrain|fatScalp}$ did not enhance the 2HG tumor contrast in this patient, it reduced the random foci of high 2HG background outside the tumor that were noticed with the $2SH_{Box}$ shim. This result has also been replicated in healthy volunteers.

In a recent study[11] that compared dual refocusing (PRESS, TE = 97 ms) and J-difference (MEGA-PRESS, TE = 68 ms) for 2HG detection, the dual-refocusing scheme required lower CRLB for an acceptable predictive value. In MRSI applications, CRLB of up to 50% for 2HG may be acceptable, because a cluster of voxels is typically obtained, and each voxel adds information about the presence or absence of 2HG. In single voxel spectroscopy (SVS), narrower spectral linewidths are usually obtained, and due to the lack of information from multiple locations, the CRLB threshold may need to be set as lower (e.g. 20%). The AC/DC shimming may enable this performance over larger brain volumes, for challenging tumor locations, and for a wider range of scanner platforms. The AC/DC coil allows 2HG imaging of an unrestricted FOV of the brain slab in a faster time (5 min 24 s) that is clinically more feasible compared with previous 3D (18 min 22 s in[14] and 19 min in[16]) and 2D (13 min 20 s in[15]) 2HG imaging.

We demonstrate the utility of using convex optimization to jointly solve for the tailored B_0 offset field and the HGSB inversion pulse transition frequency. While realized here using an integrated AC/DC coil array, any hardware capable of rapidly switchable local field control could be adapted for this application, such as spherical harmonics or stand-alone multicoil shim arrays. The lipid suppression depends on how well the specific shim coil can tailor the B_0 field offsets to the specific skull shape of the subject, which improves with more degrees of freedom. Alternatively, it was recently shown by de Graaf et al.[30] that using only a small number of high-amplitude pulsed 2SH coils improved lipid suppression by creating an elliptical B_0 field that approximates the shape of the skull for single-slice MRSI, but may be challenging for a thick slab. Another hardware approach to lipid suppression includes a dedicated lipid crusher coil[31] that creates a spoiling B_0 field pattern in the scalp, but cannot improve B_0 homogeneity in the brain.

We note that there are several differences in the shim calculation between our $2SH_{Box}$ + $ACDC_{metBrain|fatScalp}$ method and the vendor-provided $2SH_{Box}$ shimming routine of our scanner: the B_0 fieldmap sequences, the phase unwrapping algorithm, and the shim volume. Therefore, the reported improvements potentially stem not only from the AC/DC hardware itself, but also from the shim software and volume. We investigated this issue in supporting information file S6. In addition to,[28] we incorporated a navigator into our MRSI sequence

for real-time B_0 field mapping to correct frequency drift and motion, as well as monitoring the stability of the AC/DC hardware.

Our study has some limitations. Although we performed immunohistochemistry staining in biopsies of all four tumor patients, we do not have ground truth 2HG concentrations, because immunohistochemistry staining cannot be used to determine 2HG levels. A meaningful validation would require a comparison between in vivo 2HG imaging and mass spectroscopy 2HG measurements from multiple biopsies collected throughout the entire volume of the brain, and ideally also outside the tumor in the normal appearing brain. Because this is not yet possible for us, we cannot verify our measured 2HG concentrations. Instead, we compared the spatial distribution of high 2HG concentrations with the FLAIR tumor hyperintensity, and noticed that there is greater agreement between high 2HG regions and FLAIR lesions in the case of 2SH + ACDC shimming. However, our presented 2HG maps show 2HG concentrations above zero also in regions outside the FLAIR-enhancing tumors. The reasons for this are unclear, but might be technical or biological in nature. Technical reasons may be related to residual lipid artifacts, which are fitted as 2HG. Further variability may be introduced by spiral-related artifacts, such as temporal interleaving artifacts, artifacts related to RF imperfections, the variability in tCr that is used for our absolute concentration estimates, or the point-spread function caused by the spiral acquisition and the used Hamming filter. The latter, in particular, may make 2HG foci (coinciding with the tumors, but also outside) appear larger than they are. It is also important to note that our absolute concentration values of 2HG are in fact only institutional units, due to the assumption of tCr concentration values, as well as T1- and T2-relaxation times. Furthermore, the study only shows improvements when using the AC/DC coil for our scanner, our choice of shim volumes, and our shim methodology. It is not clear how these results generalize to other settings. We limited the 3D coverage to a brain slab of 5-cm thickness because larger slabs strongly reduce the achievable separation between brain metabolites and scalp lipids during the $2SH_{Box} + ACDC_{fatScalp}$ shim, and also degrade achievable B_0 homogeneity during the $2SH_{Box} + ACDC_{metBrain}$ shim. However, our MRSI sequence is not limited to 5 cm, and a larger slab can be encoded within the same acquisition time. The AC/DC coil used a pre-existing loop geometry that was optimized for RF reception, rather than local B_0 field control. A coil explicitly designed to jointly optimize RF reception, B_0 homogeneity, and tailored lipid suppression may improve performance for thicker brain slabs. Furthermore, the B_0-calibration of the individual AC/DC coils might be biased and noisy, thus limiting the achieved B_0-fidelity. Improved B_0-calibration sequences[23] might further enhance our method in the future. Although it is not possible with our data to discriminate between improvements achieved by narrower linewidths or by improved lipid suppression, such a comparison has been performed in volunteers, and showed that both improvements are equally important.[28] Also, our methodology does not improve lipid suppression above 2.24 ppm, but the $2SH_{Box} + ACDC_{fatScalp}$ can partially achieve inversion of lipid peaks of 2.25 ppm or less. Another limitation is that we did not jointly optimize the $2SH_{Box}$ shim with the $ACDC_{fatScalp}$ or the $ACDC_{metBrain}$ because the second-order 2SH shim currents of the scanner cannot be updated rapidly enough to dynamically switch with the $ACDC_{metBrain}$ and the $ACDC_{fatScalp}$.

5 | CONCLUSIONS

Integrated RF-receive and B_0-shim coil arrays can improve the spectral linewidth and lipid suppression for 3D MRSI of human brain in patients and healthy volunteers at 3 T. This facilitates the use of low-resolution MRSI to shorten the acquisition time and gain SNR for 2HG imaging, without the artifacts associated with low resolution and unrestricted FOV (i.e. broad spectral linewidths and lipid contamination). We show that the combination of dynamic AC/DC multicoil shimming, real-time navigators for motion and frequency correction, and optimized 3D MRSI for 2HG detection, is feasible in mutant IDH glioma patients, and hence has high potential for clinical translation. This methodology resulted in higher CNR for 2HG images, and a more reliable detection of 2HG inside the tumors. AC/DC coils complement other methods, and thus improve already optimized methods for 2HG detection or other metabolites. We expect that this novel methodology will enable precision oncology in glioma patients for treatment planning[2] and assessment of treatment response to targeted therapies.[1,3,5] Furthermore, this methodology is applicable to the study of other neurological diseases or in healthy subjects.

Supplementary Material

Refer to Web version on PubMed Central for supplementary material.

DATA AVAILABILITY STATEMENT

The data that support the findings of this study are available from the corresponding author upon reasonable request.

Abbreviations used:

2HG	D-2-hydroxyglutarate
2SH	second-order spherical harmonics
ASE	adiabatic spin echo
CNR	contrast-to-noise ratio
CRLB	Cramér–Rao lower bounds

| CV	coefficient of variation
DESS	dual echo steady state
FLAIR	FLuid-Attenuated Inversion Recovery
FOV	field of view
Glx	glutamate and glutamine
GOIA-W	GOIA-WURST gradient offset independent wideband uniform rate and smooth truncation
HGSB	hypergeometric single band
IDH	isocitrate dehydrogenase
MEMPRAGE	multiecho magnetization prepared rapid gradient echo
MRSI	magnetic resonance spectroscopic imaging
RF	radio frequency
ROI	region of interest
SNR	signal-to-noise ratio
SVS	single voxel spectroscopy
tCr	total creatine
TI	inversion time
tNAA	total N-acetyl aspartate
WET	water suppression enhanced through T_1 effects

REFERENCES

1. Andronesi OC, Arrillaga-Romany IC, Ly KI, et al. Pharmacodynamics of mutant-IDH1 inhibitors in glioma patients probed by in vivo 3D MRS imaging of 2-hydroxyglutarate. Nat Commun. 2018;9(1):1474–1483. [PubMed: 29662077]

2. Jafari-Khouzani K, Loebel F, Bogner W, et al. Volumetric relationship between 2-Hydroxyglutarate and FLAIR hyperintensity has potential implications for radiotherapy planning of mutant IDH glioma patients. Neuro Oncol. 2016;18(11):1569–1578. [PubMed: 27382115]

3. Andronesi OC, Loebel F, Bogner W, et al. Treatment response assessment in IDH-mutant glioma patients by non-invasive 3D functional spectroscopic mapping of 2-hydroxyglutarate. Clin Cancer Res. 2016;22(7):1632–1641. [PubMed: 26534967]

4. de la Fuente MI, Young RJ, Rubel J, et al. Integration of 2-hydroxyglutarate-proton magnetic resonance spectroscopy into clinical practice for disease monitoring in isocitrate dehydrogenase-mutant glioma. Neuro Oncol. 2016;18(2):283–290. [PubMed: 26691210]

5. Choi C, Raisanen JM, Ganji SK, et al. Prospective longitudinal analysis of 2-hydroxyglutarate magnetic resonance spectroscopy identifies broad clinical utility for the management of patients with IDH-mutant glioma. J Clin Oncol. 2016;34(33):4030–4039. [PubMed: 28248126]

6. Dang L, White DW, Gross S, et al. Cancer-associated IDH1 mutations produce 2-hydroxyglutarate. Nature. 2009;462(7274):739–744. [PubMed: 19935646]

7. Parsons DW, Jones S, Zhang XS, et al. An integrated genomic analysis of human glioblastoma Multiforme. Science. 2008;321(5897):1807–1812. [PubMed: 18772396]

8. Andronesi OC, Kim GS, Gerstner E, et al. Detection of 2-hydroxyglutarate in IDH-mutated glioma patients by in vivo spectral-editing and 2D correlation magnetic resonance spectroscopy. Sci Transl Med. 2012;4(116):116ra4.

9. Choi C, Ganji SK, DeBerardinis RJ, et al. 2-hydroxyglutarate detection by magnetic resonance spectroscopy in subjects with IDH-mutated gliomas. Nat Med. 2012;18(4):624–629. [PubMed: 22281806]

10. Berrington A, Voets NL, Plaha P, et al. Improved localisation for 2-hydroxyglutarate detection at 3T using long-TE semi-LASER. Tomography. 2016; 2(2):94–105. [PubMed: 27547821]

11. Branzoli F, Di Stefano AL, Capelle L, et al. Highly specific determination of IDH status using edited in vivo magnetic resonance spectroscopy. Neuro Oncol. 2018;20(7):907–916. [PubMed: 29126125]

12. An Z, Ganji SK, Tiwari V, et al. Detection of 2-hydroxyglutarate in brain tumors by triple-refocusing MR spectroscopy at 3T in vivo. Magn Reson Med. 2017;78(1):40–48. [PubMed: 27454352]

13. Choi C, Ganji S, Hulsey K, et al. A comparative study of short- and long-TE (1)H MRS at 3 T for in vivo detection of 2-hydroxyglutarate in brain tumors. NMR Biomed. 2013;26(10):1242–1250. [PubMed: 23592268]

14. Li X, Strasser B, Jafari-Khouzani K, et al. Super-resolution whole-brain 3D MR spectroscopic imaging for mapping D-2-hydroxyglutarate and tumor metabolism in isocitrate dehydrogenase 1-mutated human gliomas. Radiology. 2020;294(3):589–597. [PubMed: 31909698]

15. Steel A, Chiew M, Jezzard P, et al. Metabolite-cycled density-weighted concentric rings k-space trajectory (DW-CRT) enables high-resolution 1 H magnetic resonance spectroscopic imaging at 3-Tesla. Sci Rep. 2018;8(1):7792–7802. [PubMed: 29773892]

16. An Z, Tiwari V, Baxter J, et al. 3D high-resolution imaging of 2-hydroxyglutarate in glioma patients using DRAG-EPSI at 3T in vivo. Magn Reson Med. 2019;81(2):795–802. [PubMed: 30277274]

17. Aghaeifar A, Mirkes C, Bause J, et al. Dynamic B0 shimming of the human brain at 9.4 T with a 16-channel multi-coil shim setup. Magn Reson Med. 2018;80(4):1714–1725. [PubMed: 29424461]

18. Pan JW, Lo KM, Hetherington HP. Role of very high order and degree B0 shimming for spectroscopic imaging of the human brain at 7 Tesla. Magn Reson Med. 2012;68(4):1007–1017. [PubMed: 22213108]

19. Juchem C, Nixon TW, McIntyre S, Boer VO, Rothman DL, de Graaf RA. Dynamic multi-coil shimming of the human brain at 7 T. J Magn Reson. 2011; 212(2):280–288. [PubMed: 21824794]

20. Stockmann JP, Witzel T, Keil B, et al. A 32-channel combined RF and B0 shim array for 3T brain imaging. Magn Reson Med. 2016;75(1):441–451. [PubMed: 25689977]

21. Truong TK, Darnell D, Song AW. Integrated RF/shim coil array for parallel reception and localized B0 shimming in the human brain. Neuroimage. 2014; 103:235–240. [PubMed: 25270602]

22. Fillmer A, Kirchner T, Cameron D, Henning A. Constrained image-based B0 shimming accounting for "local minimum traps" in the optimization and field inhomogeneities outside the region of interest. Magn Reson Med. 2015;73(4):1370–1380. [PubMed: 24715495]

23. Hetherington HP, Chu WJ, Gonen O, Pan JW. Robust fully automated shimming of the human brain for high-field 1H spectroscopic imaging. Magn Reson Med. 2006;56(1):26–33. [PubMed: 16767750]

24. Kirchner T, Fillmer A, Henning A. Mechanisms of SNR and line shape improvement by B0 correction in overdiscrete MRSI reconstruction. Magn Reson Med. 2017;77(1):44–56. [PubMed: 26860614]

25. Ebel A, Maudsley AA, Schuff N. Correction of local B0 shifts in 3D EPSI of the human brain at 4 T. Magn Reson Imaging. 2007;25(3):377–380. [PubMed: 17371727]

26. Liu Y, Ma C, Clifford B, Lam F, Johnson CL, Liang ZP. Field-inhomogeneity-corrected low-rank filtering of magnetic resonance spectroscopic imaging data. IEEE Eng Med Biol Soc Annual Conf. 2014;2014:6422–6425.

27. Juchem C, Green D, de Graaf RA. Multi-coil magnetic field modeling. J Magn Reson. 2013;236:95–104. [PubMed: 24095841]

28. Arango N, Stockman J & Strasser B et al. Dynamically switched B0 field control for separate optimization of tailored volume lipid suppression and B0 homogeneity for brain chemical shift imaging at 3T using multi-coil shim array. Proceedings of the 26th Annual Meeting of ISMRM, Paris, France; 2018. Abstract #1062.

29. Esmaeili M, Stockmann J, Strasser B, et al. An integrated RF-receive/B(0)-shim array coil boosts performance of whole-brain MR spectroscopic imaging at 7 T. Sci Rep. 2020;10(1):15029–15046. [PubMed: 32929121]

30. de Graaf RA, Brown PB, De Feyter HM, McIntyre S, Nixon TW. Elliptical localization with pulsed second-order fields (ECLIPSE) for robust lipid suppression in proton MRSI. NMR Biomed. 2018;31(9):e3949. [PubMed: 29985532]

31. Boer VO, van de Lindt T, Luijten PR, Klomp DW. Lipid suppression for brain MRI and MRSI by means of a dedicated crusher coil. Magn Reson Med. 2015;73(6):2062–2068. [PubMed: 24947343]

32. Arango N, Stockmann JP, Witzel T, Wald L & White J Open-source, low-cost, flexible, current feedback-controlled driver circuit for local B0 shim coils and other applications. Proceedings of the 24th ISMRM Scientific Meeting, 3–7 May, Singapore; 2016. Abstract #1157.

33. Jenkinson M Fast, automated, N-dimensional phase-unwrapping algorithm. Magn Reson Med. 2003;49:193–197. [PubMed: 12509838]

34. Esmaeili M, Bathen TF, Rosen BR, Andronesi OC. Three-dimensional MR spectroscopic imaging using adiabatic spin echo and hypergeometric dualband suppression for metabolic mapping over the entire brain. Magn Reson Med. 2017;77(2):490–497. [PubMed: 26840906]

35. Degraaf RA, Luo Y, Terpstra M, Merkle H, Garwood M. A new localization method using an adiabatic pulse, Bir-4. J Magn Reson B. 1995;106(3): 245–252. [PubMed: 7719624]

36. Andronesi OC, Ramadan S, Ratai EM, Jennings D, Mountford CE, Sorensen AG. Spectroscopic imaging with improved gradient modulated constant adiabaticity pulses on high-field clinical scanners. J Magn Reson. 2010;203(2):283–293. [PubMed: 20163975]

37. Rosenfeld D, Panfil SL, Zur Y. Design of selective adiabatic inversion pulses using the adiabatic condition. J Magn Reson. 1997;129(2):115–124. [PubMed: 9441875]

38. Ebel A, Govindaraju V, Maudsley AA. Comparison of inversion recovery preparation schemes for lipid suppression in H-1 MRSI of human brain. Magn Reson Med. 2003;49(5):903–908. [PubMed: 12704773]

39. Ogg RJ, Kingsley PB, Taylor JS. WET, a T-1-insensitive and B-1-insensitive water-suppression method for in-vivo localized H-1-NMR spectroscopy. J Magn Reson B. 1994;104(1):1–10. [PubMed: 8025810]

40. Bogner W, Hess AT, Gagoski B, et al. Real-time motion- and B-correction for LASER-localized spiral-accelerated 3D-MRSI of the brain at 3T. Neuroimage. 2013;88C:22–31.

41. van der Kouwe AJW, Benner T, Salat DH, Fischl B. Brain morphometry with multiecho MPRAGE. Neuroimage. 2008;40(2):559–569. [PubMed: 18242102]

42. Mayer D, Levin YS, Hurd RE, Glover GH, Spielman DM. Fast metabolic imaging of systems with sparse spectra: application for hyperpolarized 13C imaging. Magn Reson Med. 2006;56(4):932–937. [PubMed: 16941617]

43. Hoge RD, Kwan RK, Pike GB. Density compensation functions for spiral MRI. Magn Reson Med. 1997;38(1):117–128. [PubMed: 9211387]

44. Beatty PJ, Nishimura DG, Pauly JM. Rapid gridding reconstruction with a minimal oversampling ratio. IEEE Trans Med Imaging. 2005;24(6):799–808. [PubMed: 15959939]

45. Provencher SW. Estimation of metabolite concentrations from localized in-vivo proton NMR-spectra. Magn Reson Med. 1993;30(6):672–679. [PubMed: 8139448]

46. Smith SA, Levante TO, Meier BH, Ernst RR. Computer-simulations in magnetic-resonance - an object-oriented programming approach. J Magn Reson A. 1994;106(1):75–105.

47. de Graaf RA, Rothman DL. In vivo detection and quantification of scalar coupled 1H NMR resonances. Concepts Magn Reson. 2001;13(1):32–76.

48. Smith SM, Jenkinson M, Woolrich MW, et al. Advances in functional and structural MR image analysis and implementation as FSL. Neuroimage. 2004; 23(Suppl 1):S208–S219. [PubMed: 15501092]

49. Govindaraju V, Young K, Maudsley AA. Proton NMR chemical shifts and coupling constants for brain metabolites. NMR Biomed. 2000;13(3):129–153. [PubMed: 10861994]

50. Bal D, Gryff-Keller A. 1H and 13C NMR study of 2-hydroxyglutaric acid and its lactone. Magn Reson Chem. 2002;40(8):533–536.

51. Capper D, Zentgraf H, Balss J, Hartmann C, von Deimling A. Monoclonal antibody specific for IDH1 R132H mutation. Acta Neuropathol. 2009;118(5): 599–601. [PubMed: 19798509]
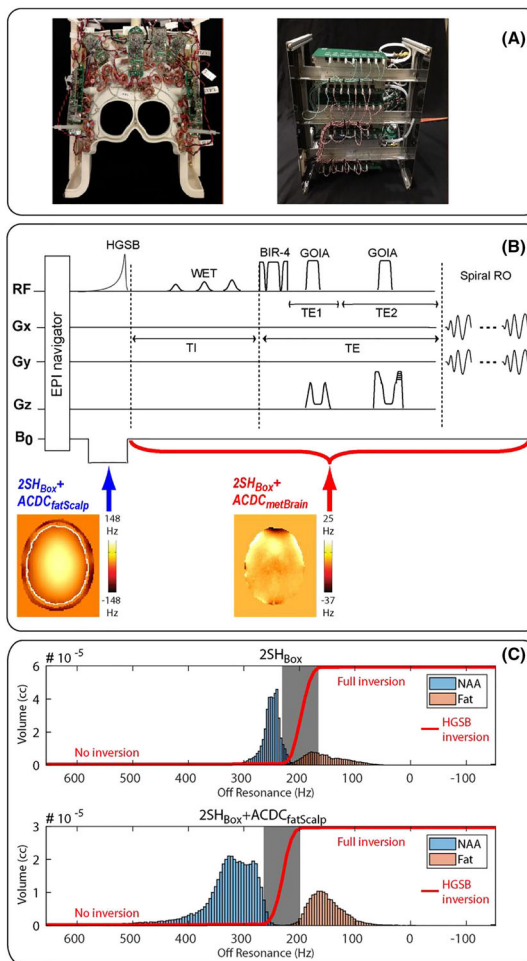
FIGURE 1.

(A) 32-channel AC/DC coil (left) and shim control boards (right); (B) Pulse sequence diagram showing the dynamic shim update. Arrows indicate the times at which the different dynamic shims are applied; (C) Histogram of fat and N-acetyl aspartate (NAA) frequency distribution in the scalp layer and brain compartment, respectively, for standard $2SH_{Box}$ shimming (top) and fat suppression shimming (bottom). The hypergeometric single band (HGSB) inversion profile is shown by the red line and the transition band by the gray boxes. An offset of 0 Hz corresponds to the frequency of tetramethylsilane
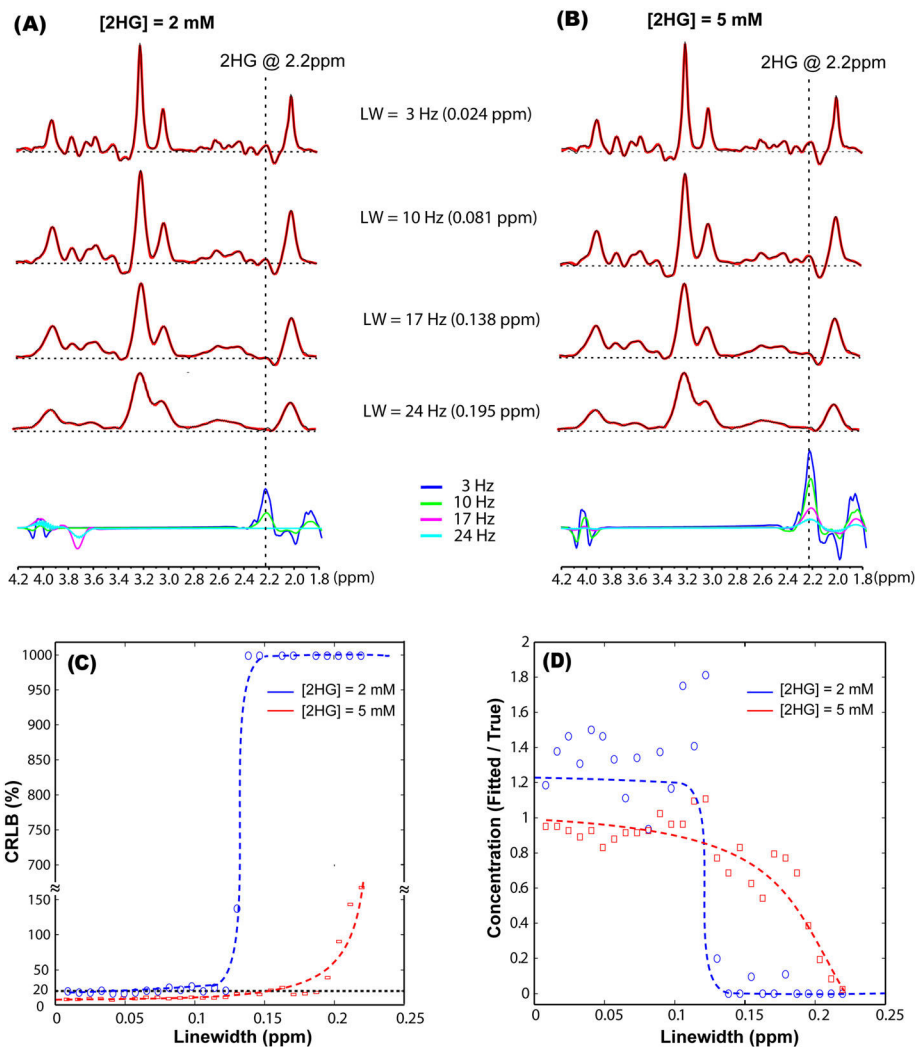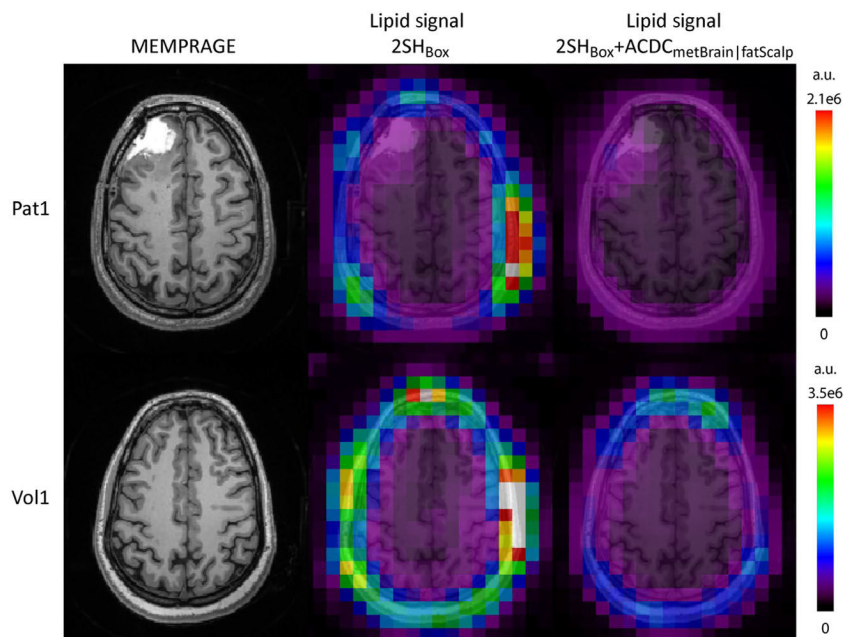
FIGURE 2.

Effect of increasing the linewidth on fitting simulated brain tumor spectra that contained 14 brain metabolites and D-2-hydroxyglutarate (2HG): (A) Tumor spectra containing 2 mM 2HG, and (B) Tumor spectra containing 5 mM 2HG. The effect of increasing linewidths on the precision and accuracy of 2HG quantification in simulated spectra: (C) Cramér–Rao lower bounds (CRLB) values are indicative of precision, and (D) the ratio between the true and fitted concentration is indicative of accuracy. Spectra were simulated in GAMMA for the ASE sequence assuming TE = 97 ms (TE1/TE2 = 32/65 ms) and a 3-T B_0 field. LCModel fitting (A, B) is shown in red overlaid on the simulated spectra shown in black in the upper four rows, and below, the fitted 2HG contribution in each spectrum is shown for the four linewidths. Trend lines (dashed) are shown in (C, D), and the 20% CRLB threshold for goodness of fit is indicated by the dashed line in (C), while the ground truth value is shown by the dashed line drawn at 1 in (D)
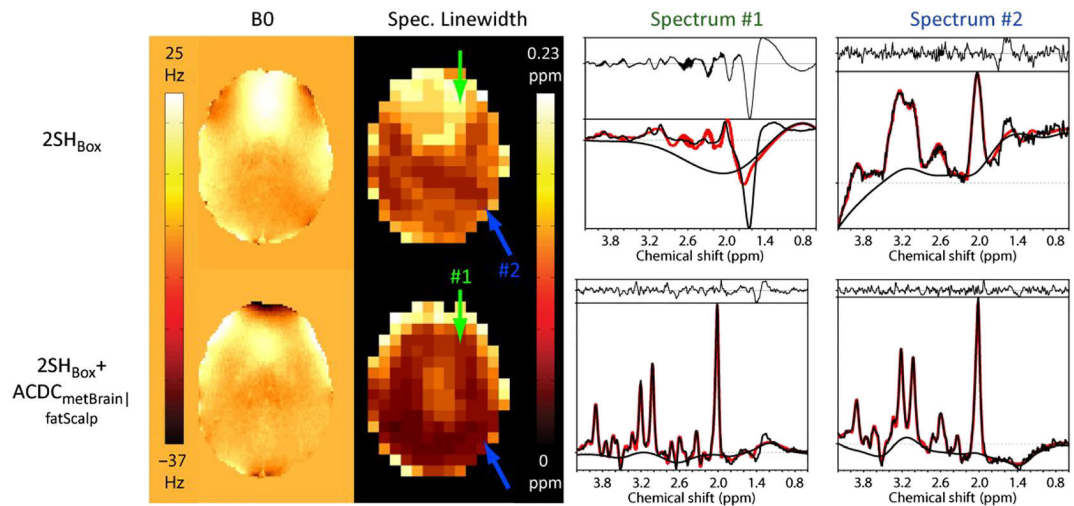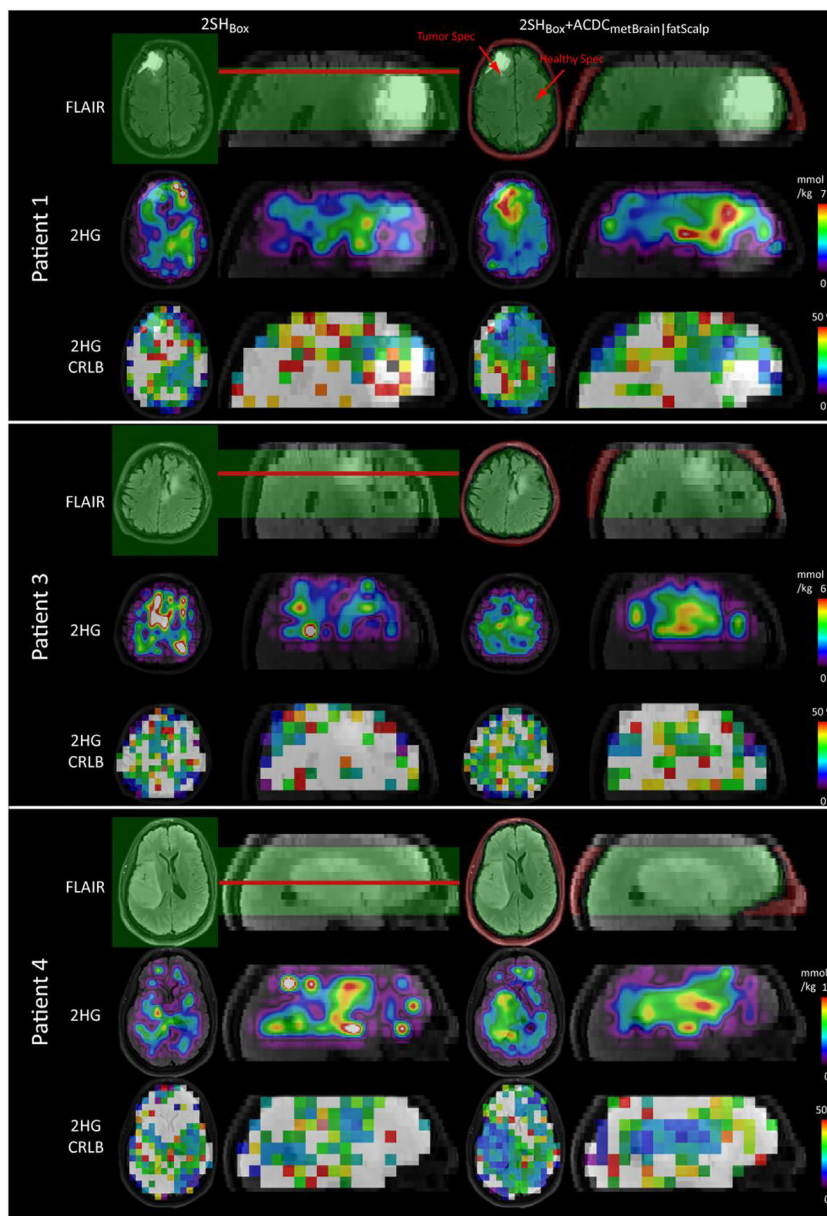
FIGURE 3.

Measured B_0-maps of patient 2 acquired with the $2SH_{Box}$ and with the $2SH_{Box}$ + $ACDC_{metBrain}$ (first column). As a result of the higher B_0-homogeneity, the average spectral linewidth was decreased with the $2SH_{Box}$ + $ACDC_{metBrain|fatScalp}$ (second column). Arrows indicate the position of the sample spectra (right two columns). The $2SH_{Box}$ + $ACDC_{metBrain|fatScalp}$ spectrum #1 shows significantly narrower linewidth, while spectrum #2 displays narrower linewidth and a flatter baseline due to the improved lipid and water suppression in the dynamic $2SH_{Box}$ + $ACDC_{metBrain|fatScalp}$ condition. Fat contamination is especially visible in spectrum #1 with $2SH_{Box}$. LCModel fitting shown in red is overlaid on the measured spectra (black)
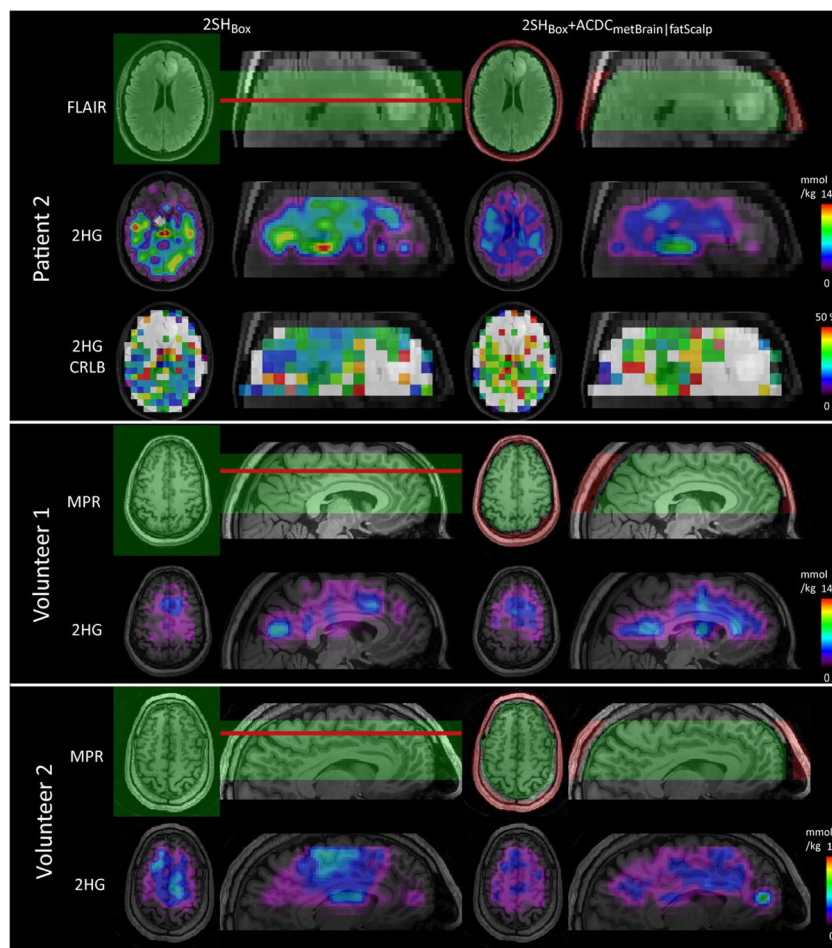
FIGURE 4.

Lipid maps for the standard $2SH_{Box}$ shim and the $2SH_{Box} + ACDC_{metBrain|fatScalp}$ for patient 1 and volunteer 1 together with the MEMPRAGE images. A decrease in the lipid content is clearly visible for both subjects for the $2SH_{Box} + ACDC_{metBrain|fatScalp}$ in comparison with the 2SH shim. The lipids in $2SH_{Box} + ACDC_{metBrain|fatScalp}$ were decreased to 0.43 ± 0.49 (mean $\pm$ std) of the $2SH_{Box}$ values for those two subjects. Lipid maps are given in arbitrary units
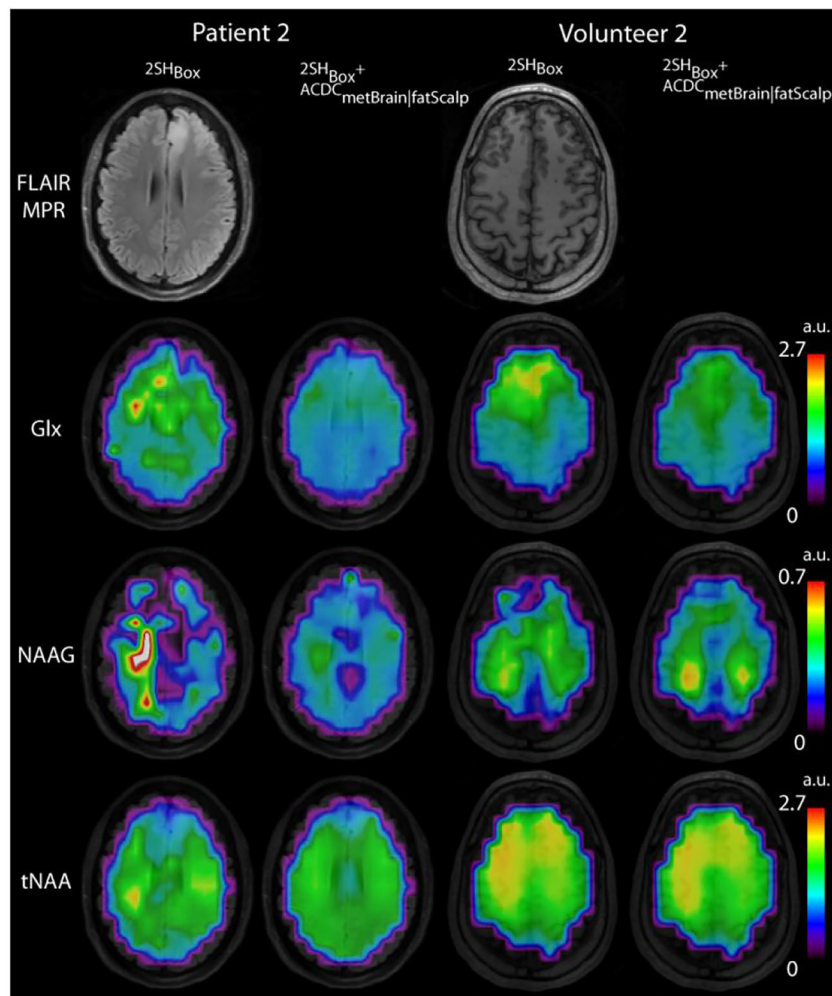
FIGURE 5.

D-2-hydroxyglutarate (2HG) maps obtained by $2SH_{Box}$ shim and the $2SH_{Box}$ + $ACDC_{metBrain|fatScalp}$ in patients 1, 3, and 4. Absolute 2HG concentrations were calculated by normalizing to the mean total creatine (tCr) signal. Cramér–Rao lower bounds (CRLB) maps are shown with 50% maximum threshold. Low CRLB in the tumor are obtained in particular with the $2SH_{Box}$ + $ACDC_{metBrain|fatScalp}$. Red arrows indicate the spectra location shown in Figure S2. The shim volumes are shown in green ($2SH_{Box}$ and $ACDC_{metBrain}$) and red ($ACDC_{fatScalp}$) overlaid on the FLAIR. The red lines indicate the positions of the shown transverse slices. 2HG maps with the native resolution are shown in supporting information file S9 together with the interpolated resolution

FIGURE 6.

D-2-hydroxyglutarate (2HG) maps obtained by $2SH_{Box}$ shim and the $2SH_{Box}$ + $ACDC_{metBrain|fatScalp}$ in patient 2 and volunteers 1 and 2. With standard $2SH_{Box}$ shimming, high 2HG foci can be seen in random locations throughout healthy brain and far from the tumor in the patient. The 2HG maps show fewer remote foci outside the tumors with the $2SH_{Box}$ + $ACDC_{metBrain|fatScalp}$ shim. Patient 2 had a low-grade small tumor with a very low density of mutant IDH1-R132H cells and its 2HG levels are expected to be very close to the normal background. The shim volumes are shown in green ($2SH_{Box}$ and $ACDC_{metBrain}$) and red ($ACDC_{fatScalp}$) overlaid on the FLAIR or MEMPRAGE. The red lines indicate the positions of the shown transverse slices. 2HG maps with the native resolution are shown in supporting information file S9 together with the interpolated resolution

FIGURE 7.

Glx, NAAG, and tNAA maps for volunteer 2 and patient 2 overlaid on MEMPRAGE images. This figure shows a clear improvement in metabolic maps other than 2HG when using the $2SH_{Box} + ACDC_{metBrain|fatScalp}$ shim compared with the $2SH_{Box}$ shim only. In patient 2 there is more spatial variability in $2SH_{Box}$ metabolic maps with foci of high and low intensity in random locations, while $2SH_{Box} + ACDC_{metBrain|fatScalp}$ metabolic maps correspond better to brain anatomy and tumor location. Volunteer 2 provides an example of where the improvement by the $2SH_{Box} + ACDC_{metBrain|fatScalp}$ shim is smaller, because the data quality was already sufficient in the 2SH case. Glx, glutamate + glutamine; NAAG, N-acetylaspartylglutamic acid; tNAA, NAA + N-acetyl-aspartyl-glutamate

TABLE 1

Comparison of parameters obtained with standard vendor implemented $2SH_{Box}$ shimming alone and with the combined $2SH_{Box} + ACDC_{metBrain|fatScalp}$ shimming

Shim method		# Vox []	LW [ppm]	SNR []	Fat [%]	2HG tumor CRLB [%]	2HG tumor CNR []
$2SH_{Box}$	Vol	2210	0.091 ± 0.041	16.1 ± 6.9	100 ± 158	N/A	N/A
	Pat	1475	0.098 ± 0.043	14.2 ± 6.5	100 ± 167	300 ± 430	0.11 ± 0.05
$2SH_{Box} +$ $ACDC_{metBrain|fatScalp}$	Vol	2210	0.074 ± 0.036	17.6 ± 6.7	79 ± 130	N/A	N/A
	Pat	1475	0.080 ± 0.041	13.9 ± 6.0	30 ± 39	39 ± 74	1.45 ± 0.74

Note: Numbers for LW, SNR, and fat contamination represent mean and std (where applicable) values averaged over either patients (Pat) or volunteers (Vol) and all brain voxels. The fat contamination was calculated relative to standard $2SH_{Box}$ shimming, which was assumed to have 100% contamination. The values for CRLB were calculated for 2HG only in the tumor areas of patients 1, 3, and 4 that have detectable 2HG levels by MRSI. Similarly, the CNR was calculated based on the patients 1, 3, and 4 with detectable 2HG levels by MRSI.

Abbreviations: 2HG, D-2-hydroxyglutarate; CNR, contrast-to-noise ratio; CRLB, Cramér–Rao lower bounds; Fat, contamination with scalp lipid signals; LW, linewidth; SNR, signal-to-noise ratio.

Vox, the number of total voxels pooled over all considered subjects.